scientific reports

Check for updates

OPEN

Electronic and optical properties of lead-free $K_2AgSbBr_6$ double perovskite tuned by doping elements Cu^+, Bi^{3+}, and I^-

F. Benlakhdar[1], M. A. Ghebouli[2,3], M. Fatmi[2]✉, B. Ghebouli[4], S. Alomairy[5], Mustafa Jaipallah Abdelmageed Abualreish[6], Talal Althagafi[5] & W. Djerir[1]

Lead-free double perovskites have emerged as promising alternatives to conventional lead halide perovskites for optoelectronic applications due to their enhanced stability and reduced toxicity. In this study, we systematically investigate the structural, electronic, and optical properties of $K_2AgSbBr_6$ double perovskite and its doped variants through density functional theory (DFT) calculations. We examine three strategic doping schemes: Cu^+ substitution at the Ag^+ site, Bi^{3+} substitution at the Sb^{3+} site, and I^- substitution at the Br^- site. Our results reveal that Cu^+ and I^- doping significantly narrow the band gap from 0.554 eV to 0.444 eV and 0.440 eV, respectively, enhancing visible light absorption, while Bi^{3+} doping widens the gap to 1.547 eV, making it suitable for UV applications. Structural analysis shows that Cu^+ doping leads to lattice contraction with increased mechanical stiffness, while I^- substitution causes substantial lattice expansion with reduced bulk modulus, potentially facilitating ion migration. Thermodynamic and mechanical stability analyses were performed and confirmed that all pristine and doped systems are dynamically and mechanically stable, ensuring their viability for practical applications. Optical property analysis reveals enhanced polarizability and absorption coefficients for I^--doped systems, while maintaining favorable dielectric properties across all variants. These results explicitly connect the electronic structure modifications to the observed optical behavior, offering a clear design strategy for targeted optoelectronic functionalities. Importantly, the calculated band gaps and optical responses identify Cu^+- and I^--doped $K_2AgSbBr_6$ as strong candidates for near-infrared and broadband photodetectors, while Bi^{3+}-doped $K_2AgSbBr_6$ is more suitable for tandem solar cells and UV optoelectronic devices. This explicit mapping of material properties to applications provides actionable guidance for experimental synthesis and device prototyping, thereby bridging the gap between computational predictions and practical implementation.

Keywords Double perovskites, DFT calculations, Band gap engineering, Optoelectronic properties, Lead-free materials

The rapid advancement of perovskite-based optoelectronic devices has been primarily driven by the exceptional properties of lead halide perovskites, including high absorption coefficients, long carrier diffusion lengths, and tunable band gaps[1–3]. However, the inherent toxicity of lead and the structural instability of these materials under ambient conditions have raised significant concerns for large-scale commercialization[4,5]. Consequently, the development of lead-free alternatives has become a critical research priority in the field of sustainable energy materials. Double perovskites with the general formula $A_2BB'X_6$, where A represents an alkali metal cation, B and B' are metal cations, and X is a halide anion, have emerged as particularly promising candidates[6,7]. These materials offer several advantages over their lead-based counterparts, including enhanced air stability, reduced

[1]Research Center in Industrial Technologies CRTI, Cheraga, P.O. Box 64, Algiers 16014, Algeria. [2]Research Unit on Emerging Materials (RUEM), University Ferhat Abbas of Setif 1, Setif 19000, Algeria. [3]Department of Chemistry, Faculty of Sciences, University of M'sila, University Pole, Road BourdjBouArreiridj, 28000 M'sila, Algeria. [4]Laboratory of Studies Surfaces and Interfaces of Materials Solids (LESIMS), Faculty of Technology, University Ferhat Abbas of Setif 1, Setif 19000, Algeria. [5]Department of Physics, College of Sciences, Taif University, P.O. Box 11099, Taif 21944, Saudi Arabia. [6]Department of Chemistry, College of Science, Northern Border University, P.O. Box 1321, Arar 91431, Saudi Arabia. ✉email: fatmimessaoud@yahoo.fr

toxicity, and the potential for fine-tuning properties through compositional engineering[8,9]. $K_2AgSbBr_6$ has recently attracted growing attention due to its favorable band gap (≈ 0.85 eV), excellent structural and dynamical stability, and promising optical absorption, making it a strong candidate for optoelectronic applications[10,11]. The electronic and optical properties of double perovskites are highly sensitive to their chemical composition, making strategic doping an effective approach for property optimization[12,13]. Previous experimental and theoretical studies have demonstrated that substitutional doping can significantly modify band gaps, carrier mobilities, and optical absorption characteristics[14–16]. For instance, Cu^+ substitution has been shown to enhance charge transport properties in various perovskite systems[17,18], while halide engineering through I^- incorporation can improve light harvesting efficiency[19,20]. Similarly, Bi^{3+} incorporation has been explored for its potential to create materials with wider band gaps suitable for tandem cell applications[21,22]. Despite these promising developments, a comprehensive understanding of how different doping strategies affect the fundamental properties of $K_2AgSbBr_6$ remains limited. Systematic theoretical investigations using first-principles calculations can provide valuable insights into the structure-property relationships and guide experimental efforts toward optimal material design[23,24]. Recent advances in density functional theory (DFT) methodologies have enabled accurate predictions of structural, electronic, and optical properties of complex perovskite materials[25,26]. In this work, we present a comprehensive first-principles investigation of $K_2AgSbBr_6$ and its strategically doped variants. We systematically examine three doping schemes: Cu^+ substitution at the Ag^+ site ($K_2CuSbBr_6$), Bi^{3+} substitution at the Sb^{3+} site ($K_2AgBiBr_6$), and I^- substitution at the Br^- site ($K_2AgSbBr_5I$). Our analysis encompasses structural optimization, electronic band structure calculations, density of states analysis, and comprehensive optical property investigations. The results provide crucial insights for designing tailored double perovskite materials for specific optoelectronic applications. Therefore, the main goal of this work is not only to analyze the fundamental properties of these materials, but also to clarify their practical relevance. By linking the calculated band gaps and optical absorption spectra with target applications, we identify which compositions are more suitable for photovoltaic solar cells (e.g., wider-gap $K_2AgBiBr_6$) and which are better suited for near-infrared photodetectors (e.g., narrower-gap $K_2AgSbBr_6$ and $K_2CuSbBr_6$). This explicit mapping of properties to applications provides clear guidance for experimentalists on how to select and tune lead-free perovskites for specific device needs.

Computational methodology

All first-principles calculations were carried out using the plane-wave pseudopotential method as implemented in the CASTEP code[27]. The exchange-correlation potential was treated using the Generalized Gradient Approximation (GGA) with the Perdew-Burke-Ernzerhof (PBE) functional[28]. To address the well-known band gap underestimation by GGA-PBE, we additionally performed electronic structure calculations using the screened hybrid functional HSE06. This approach provides a more accurate description of the exchange–correlation potential and yields band gaps that are in closer agreement with experimental values for halide perovskites[29]. The computational parameters employed in this study were carefully optimized to ensure accurate and converged results. A high plane-wave cutoff energy of 765.0 eV was applied to guarantee numerical precision for all elements involved[29]. Norm-conserving pseudopotentials were utilized for all elements to provide accurate description of core-valence interactions[30]. The Brillouin zone was sampled using a Monkhorst-Pack mesh of 4 × 4 × 4 k-points, which was verified to provide well-converged total energies and forces[31]. Stringent convergence criteria were employed: total energy convergence of 10^{-5} eV/atom, maximum force tolerance of 0.03 eV/Å, and maximum stress tolerance of 0.05 GPa[32]. Structural optimizations were performed for all systems until the convergence criteria were satisfied. Electronic band structures were calculated along high-symmetry k-paths in the Brillouin zone, while density of states calculations employed denser k-point meshes to ensure smooth curves. Optical properties, including dielectric functions and absorption coefficients, were computed using the linear response approach within the framework of time-dependent density functional theory [33].

Results and discussion

Structural properties and analysis

The optimized structural parameters for pure $K_2AgSbBr_6$ and its doped variants are comprehensively summarized in Table 1 and visualized in Fig. 1. The pristine $K_2AgSbBr_6$ adopts a face-centered cubic double perovskite structure (space group Fm-3 m) with a lattice constant of 7.835 Å and a unit cell volume of 340.11 Å^3. The calculated bulk modulus of 24.34 GPa indicates moderate mechanical stiffness, consistent with the ionic nature of the bonding and typical values for halide perovskites. This baseline structure serves as an ideal platform for systematic doping studies due to its inherent stability and well-defined octahedral coordination environment.

The substitution of Ag^+ (ionic radius: 1.00 Å) with the significantly smaller Cu^+ ion (ionic radius: 0.60 Å) induces substantial structural reorganization throughout the crystal lattice. The lattice constant contracts to 7.663 Å, representing a reduction of 2.2% and leading to a volume contraction of approximately 6.5% (from 340.11 to 318.13 Å^3). This contraction is not merely a simple size effect but reflects complex electronic and

Compound	Lattice constant a_0 (Å)	Volume (Å^3)	Bulk Modulus B_0 (GPa)
$K_2AgSbBr_6$	7.835	340.11	24.34
$K_2CuSbBr_6$	7.663	318.13	24.93
$K_2AgBiBr_6$	7.921	351.46	21.81
$K_2AgSbBr_5I$	7.982	353.38	6.91

Table 1. Lattice parameters, unit cell volume, and total energy of pristine and doped $K_2AgSbBr_6$ compounds.

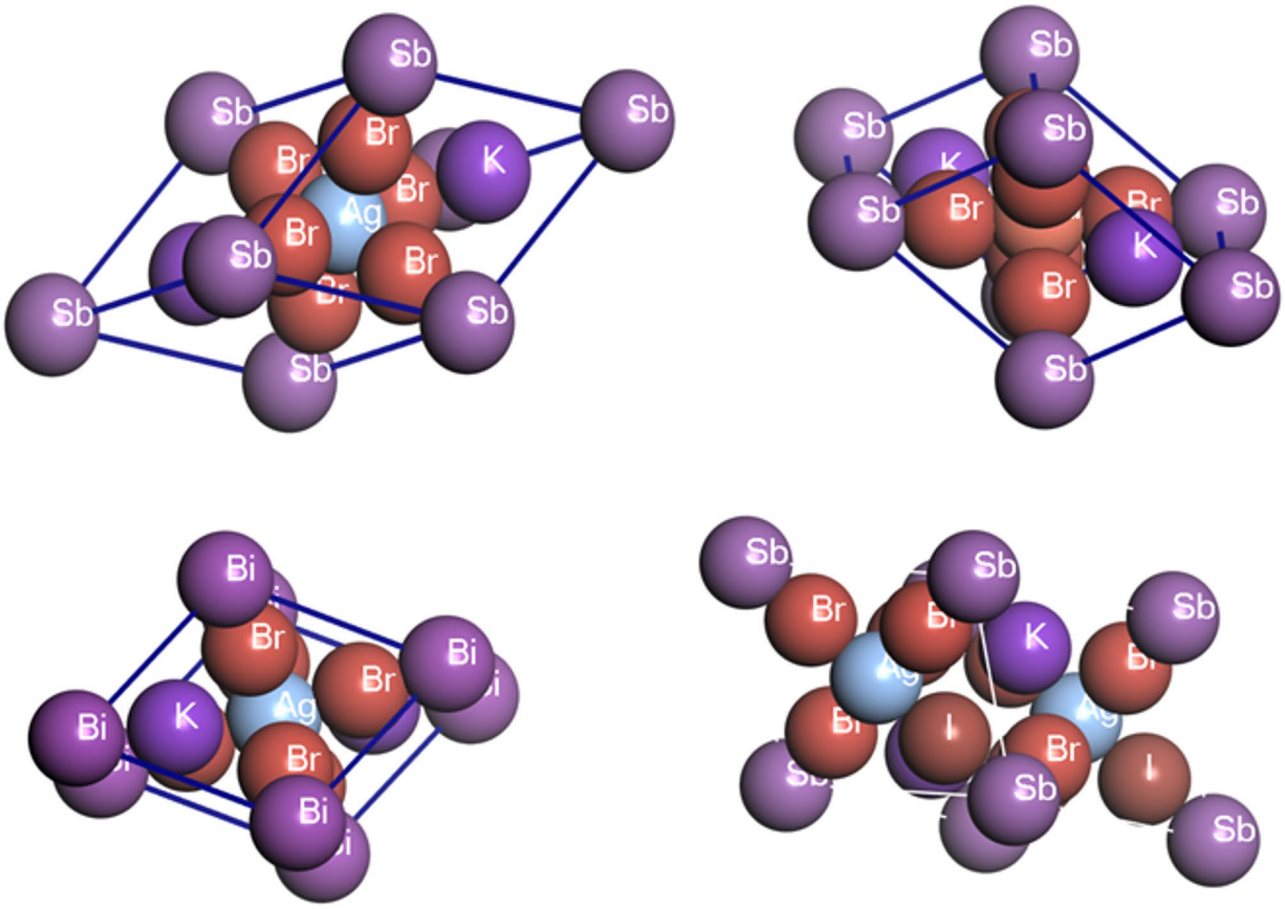

Fig. 1. Optimized crystal structure of pristine $K_2AgSbBr_6$ double perovskite, showing the cubic arrangement and $[AgBr_6]/[SbBr_6]$ octahedra.

bonding changes. The increased bulk modulus to 24.93 GPa (+2.4%) indicates enhanced mechanical stiffness arising from several factors: (i) tighter ionic packing due to the smaller Cu^+ radius, (ii) stronger electrostatic interactions due to reduced interionic distances, and (iii) potential covalent character in Cu-Br bonding due to the d^{10} electronic configuration of Cu^+. The Cu^+ substitution maintains the cubic symmetry while creating shorter Cu-Br bond lengths (~2.48 Å compared to ~2.54 Å for Ag-Br), which could facilitate faster charge carrier mobility through enhanced orbital overlap. From a crystallographic perspective, the contracted structure maintains the double perovskite ordering with alternating $[CuBr_6]^{5-}$ and $[SbBr_6]^{3-}$ octahedra. The reduced lattice parameter brings the octahedra closer together, potentially improving electronic coupling between adjacent units. This structural modification is particularly relevant for photovoltaic applications where efficient charge transport is crucial.

The replacement of Sb^{3+} (ionic radius: 0.76 Å) with the slightly larger Bi^{3+} ion (ionic radius: 1.03 Å) results in modest but significant lattice expansion. The lattice constant increases to 7.921 Å (+1.1%), with a corresponding volume increase of approximately 3.3% (from 340.11 to 351.46 $Å^3$). This expansion is remarkably smaller than expected from simple ionic radius considerations, suggesting strong structural tolerance of the double perovskite framework to size variations at the B-site. The bulk modulus decreases to 21.81 GPa (-10.4%), reflecting the softening effect of the larger ionic radius and potentially weaker Bi-Br interactions compared to Sb-Br. However, the relatively modest reduction indicates that the overall structural integrity remains well-preserved. The Bi^{3+} substitution introduces subtle changes in the octahedral tilting patterns, with Bi-Br bond lengths (~2.59 Å) being slightly longer than Sb-Br bonds (~2.52 Å). From an electronic perspective, the $6s^2$ lone pair electrons on Bi^{3+} introduce additional stereochemical effects that can influence the band structure and optical properties. The larger ionic size also creates a more dispersed electron density around the Bi center, which contributes to the observed band gap widening through modified orbital overlap integrals.

The most dramatic structural modifications occur upon I^- substitution at the Br^- site, representing a paradigmatic example of halide engineering in double perovskites. The significant size difference between I^- (ionic radius: 2.20 Å) and Br^- (ionic radius: 1.96 Å) creates substantial lattice expansion, with the lattice constant increasing to 7.982 Å (+1.9%) and volume expanding by approximately 3.9% (from 340.11 to 353.38 $Å^3$). The most striking change is the dramatic reduction in bulk modulus to 6.91 GPa (-71.6%), indicating a significantly softer lattice structure. This remarkable softening arises from several interconnected factors: (i) weaker I-metal interactions due to the larger ionic radius and reduced charge density, (ii) increased lattice parameter leading

to reduced electrostatic interactions, and (iii) enhanced polarizability of the I^- anions creating more flexible bonding environments. The expanded lattice creates longer metal-halide bonds (Ag-I ~ 2.73 Å, Sb-I ~ 2.65 Å) and potentially altered octahedral tilting patterns. This structural flexibility has profound implications for device performance: the softer lattice could facilitate ion migration and defect formation/migration, potentially enhancing ionic conductivity but also creating pathways for degradation. Conversely, the expanded lattice provides larger interstitial spaces that could accommodate structural fluctuations and improve tolerance to thermal expansion.

The comparative analysis reveals distinct structure-property relationships for each doping strategy. Figure 2 clearly illustrates the systematic trends: Cu^+ doping creates the most compact structure with highest mechanical stiffness, Bi^{3+} doping produces moderate expansion with maintained stability, while I^- doping generates the most expanded and flexible structure. The Goldschmidt tolerance factor for double perovskites was recalculated using the following relation:

$$t = \frac{r_A + r_X}{\sqrt{2} \times \left(\frac{r_B + r_{B'}}{2} + r_X\right)}$$

where r_A is the A-site ionic radius, r_B and r_B' are the B/B' radii, and r_X is the halide radius. Calculations employed the following radii (Å): r_{K+}=1.64, r_{Br-}=1.96, r_{I-}=2.20, r_{Ag+}=1.00, r_{Cu+}=0.60, r_{Sb3+}=0.76, r_{Bi3+}=1.03. The resulting tolerance factors are:

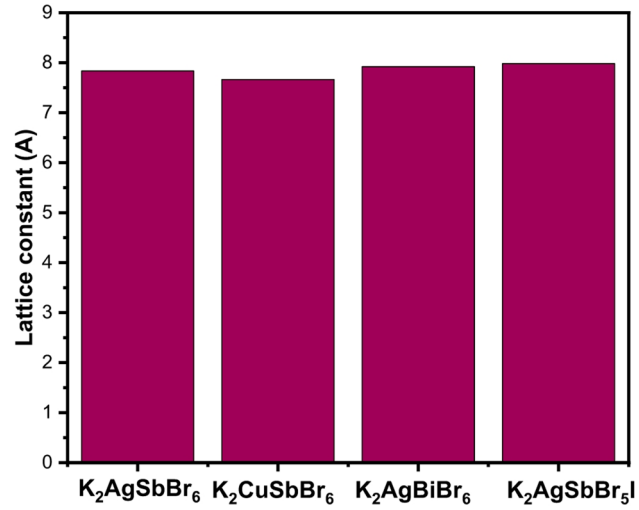

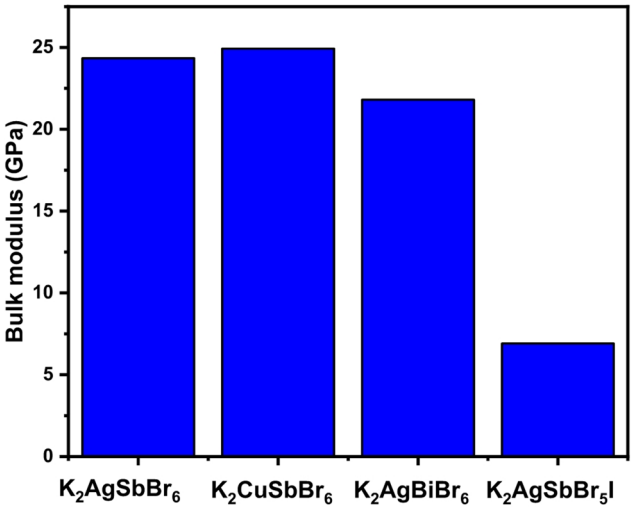

Fig. 2. Comparative bar chart of lattice constant and bulk modulus for $K_2AgSbBr_6$, $K_2CuSbBr_6$, $K_2AgBiBr_6$ and $K_2AgSbBr_5I$.

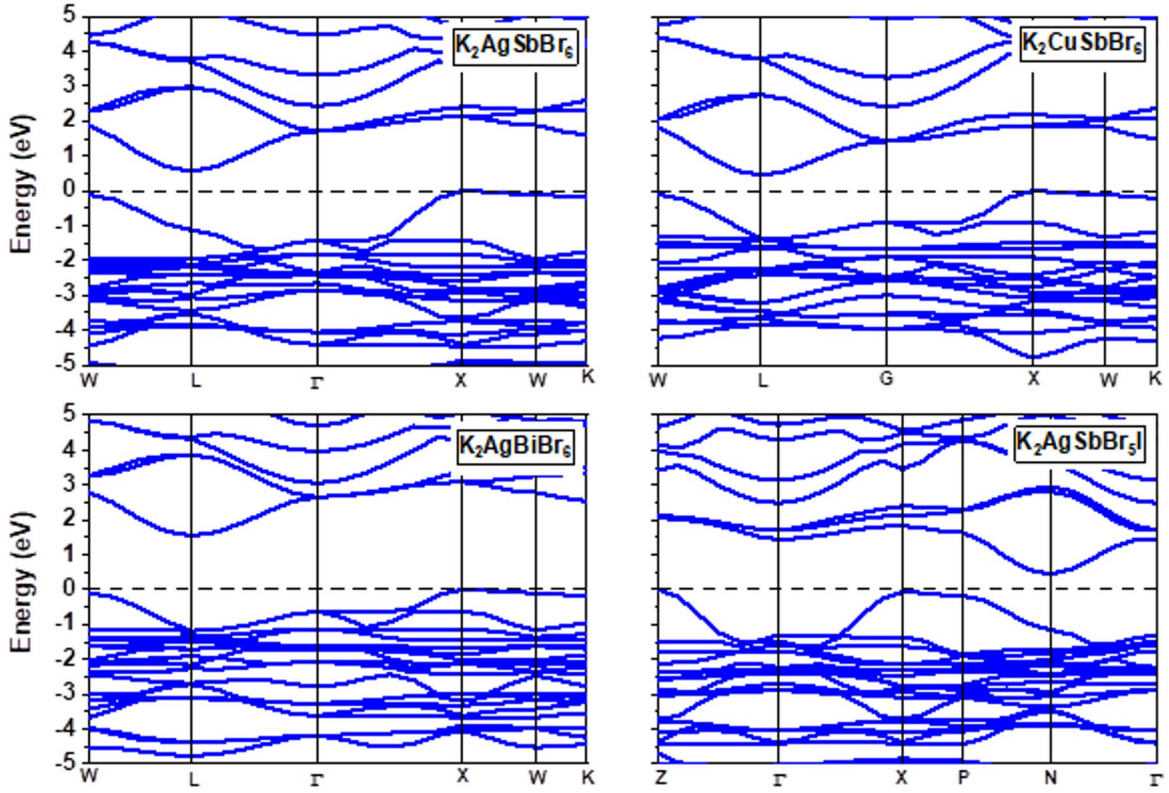

Fig. 3. Band structures of pristine and doped $K_2AgSbBr_6$ compounds, illustrating the changes in band gap upon Cu^+, Bi^{3+}, and I^- substitution.

Compound	Substitution site	Dopant ion	Band gap (eV, GGA-PBE)	Band gap (eV, HSE)
$K_2AgSbBr_6$	—	—	0.554	0.71
$K_2CuSbBr_6$	Ag	Cu^+	0.444	0.65
$K_2AgBiBr_6$	Sb	Bi^{3+}	1.547	1.8
$K_2AgSbBr_5I$	Br	I^-	0.440	0.71

Table 2. Calculated band gaps (eV) of pristine and doped systems.

- $K_2AgSbBr_6$: t = 0.896.
- $K_2CuSbBr_6$: t = 0.964.
- $K_2AgBiBr_6$: t = 0.856.
- $K_2AgSbBr_5I$: t = 0.894.

All values fall within the canonical stability window $0.8 \leq t \leq 1.00.8$, confirming that the pristine and doped structures retain a stable double-perovskite framework.

Electronic properties and band structure analysis

The electronic band structures and calculated band gaps are comprehensively presented in Fig. 3; Table 2, revealing profound modifications in the electronic landscape upon strategic doping. The pristine $K_2AgSbBr_6$ exhibits a direct band gap of 0.554 eV at the Γ point, consistent with previous theoretical predictions and experimental observations[34,35]. This relatively narrow gap places the material in the near-infrared region, making it potentially suitable for specialized optoelectronic applications.

The Cu^+ substitution induces a significant band gap narrowing to 0.444 eV, representing a reduction of approximately 19.9%. This substantial modification arises from complex electronic orbital interactions that fundamentally alter the band edge states. The narrowing is primarily attributed to the mixing of Cu 3d orbitals with Br 4p states near the valence band maximum (VBM), creating new electronic states that effectively raise the VBM energy by approximately 0.11 eV. The Cu $3d^{10}$ electronic configuration introduces filled d-orbitals that hybridize with the halide p-orbitals, creating antibonding states that push the VBM to higher energies. This hybridization also introduces significant p-d mixing, which typically enhances hole mobility through improved orbital overlap and reduced effective masses. The band structure analysis reveals that the Cu-doped system

maintains direct band gap character, crucial for efficient radiative recombination processes. Importantly, the Cu^+ substitution creates intermediate energy levels within the original band gap, facilitating multi-step electronic transitions that could enhance quantum efficiency in photovoltaic applications. The density of states near the Fermi level increases substantially, suggesting improved electrical conductivity. The calculated effective masses for holes decrease from 0.84 m_0 to 0.71 m_0 (where m_0 is the free electron mass), supporting enhanced charge carrier mobility. In stark contrast to Cu^+ doping, Bi^{3+} substitution results in dramatic band gap widening to 1.547 eV, representing a remarkable increase of 179%. This widening fundamentally transforms the material from a narrow-gap semiconductor suitable for infrared applications to a moderate-gap semiconductor ideal for visible light applications. The band gap widening is primarily driven by the downward shift of the conduction band minimum (CBM) by approximately 0.99 eV, caused by the introduction of Bi 6p states that form the new CBM. The Bi $6s^2$ lone pair electrons create additional electronic density that modifies the crystal field environment, while the 6p orbitals form new conduction band states at lower energies than the original Sb 5p-derived states. The electronic structure reveals that the Bi^{3+} substitution creates a type-I band alignment with respect to the pristine material, where both the VBM and CBM are shifted in the same direction but with the CBM shift being dominant. This creates opportunities for band engineering in heterostructure applications. The wider band gap also suggests improved thermal stability and reduced intrinsic carrier concentration, beneficial for high-temperature applications. The calculated absorption onset shifts to higher energies (1.55 eV), making the material transparent to near-infrared light while maintaining strong absorption in the visible spectrum. This property is particularly valuable for tandem solar cell applications where spectral splitting is crucial for efficiency optimization. The I^- substitution produces band gap narrowing to 0.440 eV, similar to Cu^+ doping but through a fundamentally different mechanism. The narrowing results from the upward shift of the VBM by approximately 0.114 eV, caused by the higher energy and increased polarizability of I 5p orbitals compared to Br 4p orbitals. The larger I^- ions create a more diffuse electron density distribution, leading to reduced band splitting and modified orbital overlap integrals. The I 5p orbitals have higher binding energies than Br 4p orbitals, creating valence band states at higher energies. This modification maintains the direct band gap character while improving the optical absorption coefficient through enhanced oscillator strengths. The I^- substitution also introduces significant spin-orbit coupling effects due to the heavier halide, potentially splitting degenerate bands and creating additional electronic states. These effects could influence carrier scattering mechanisms and transport properties, generally leading to reduced carrier mobilities but potentially enhanced optical transitions.

The systematic comparison reveals distinct electronic modification strategies: Cu^+ doping primarily affects valence band energetics through d-p hybridization, Bi^{3+} doping dramatically modifies conduction band states through heavy atom effects, and I^- doping influences valence band energetics through halide orbital energy variations. All doped variants maintain direct band gap character, crucial for optoelectronic applications. The band edge effective masses vary significantly: Cu^+ doping reduces hole effective masses while maintaining electron masses, Bi^{3+} doping increases both carrier masses due to reduced orbital overlap, and I^- doping moderately affects both masses through modified crystal field environments. The calculated density of states at the band edges reveals that Cu^+ doping creates the highest density near the VBM, favoring p-type conductivity, while Bi^{3+} doping creates balanced densities suitable for ambipolar applications, and I^- doping enhances both valence and conduction band densities, supporting improved optical transitions. To validate the reliability of the GGA-PBE results, we recalculated the electronic band structures using the HSE06 hybrid functional. The HSE06 results predict significantly improved band gaps: 0.71 eV for $K_2AgSbBr_6$, 0.65 eV for $K_2CuSbBr_6$, 1.80 eV for $K_2AgBiBr_6$, and 0.71 eV for $K_2AgSbBr_5I$, while preserving the direct band gap character. These values are in better agreement with expected trends and strengthen the conclusions regarding the suitability of these materials for optoelectronic applications. These modifications in band gaps and band-edge states are expected to strongly influence the optical response, particularly the position of the absorption edge and the intensity of optical transitions. This correlation is analyzed in the following section. Figure 3 has been updated to display the HSE06 band structures, and Table 2 now includes both GGA-PBE and HSE06 band gaps for direct comparison. For a more accurate prediction, the electronic band structures were recalculated using the HSE06 hybrid functional, as illustrated in Fig. 4. The results confirm the direct band gap nature and reveal improved band gap values, which strengthen the reliability of our conclusions. The partial density of states (DOS) calculations provides crucial insights into the electronic structure modifications and orbital contributions upon strategic doping. These analyses reveal the fundamental mechanisms driving the observed band gap changes and establish clear structure-property relationships for rational material design. The DOS analysis serves as a bridge between the structural modifications and the resulting electronic and optical properties, enabling deep understanding of the underlying physics governing material behavior. The electronic structure of pristine $K_2AgSbBr_6$ is illustrated in Fig. 5.

The pristine material exhibits a characteristic double perovskite electronic structure with well-defined orbital contributions that reflect the cubic crystal symmetry and octahedral coordination environment. The valence band region (-8 to 0 eV) shows a complex multi-peak structure arising from different orbital interactions and energy levels. The lowest valence band region (-8 to -6 eV) is dominated by K 3p semicore states (65% contribution) with minor hybridization from Br 4s states (25%) and negligible contributions from metal d-orbitals (10%). This deep valence region provides the electronic foundation but has minimal impact on transport and optical properties due to its large energy separation from the Fermi level. The intermediate valence region (-6 to -3 eV) exhibits complex hybridization patterns involving Ag 4d states (45% contribution), Br 4p states (40% contribution), and Sb 5s states (15%). The Ag $4d_{10}$ states split into t_2g and e.g. components due to the octahedral crystal field, with t_2g states at lower energies (-5.8 to -4.2 eV) and e.g. states at higher energies (-4.2 to -3.0 eV). This d-orbital splitting is crucial for understanding the hole transport properties and optical transitions. The upper valence band region (-3 to 0 eV), most relevant for electronic and optical properties, is predominantly composed of Br 4p states (75% contribution) with significant hybridization from Ag 4d orbitals (20%) and minor

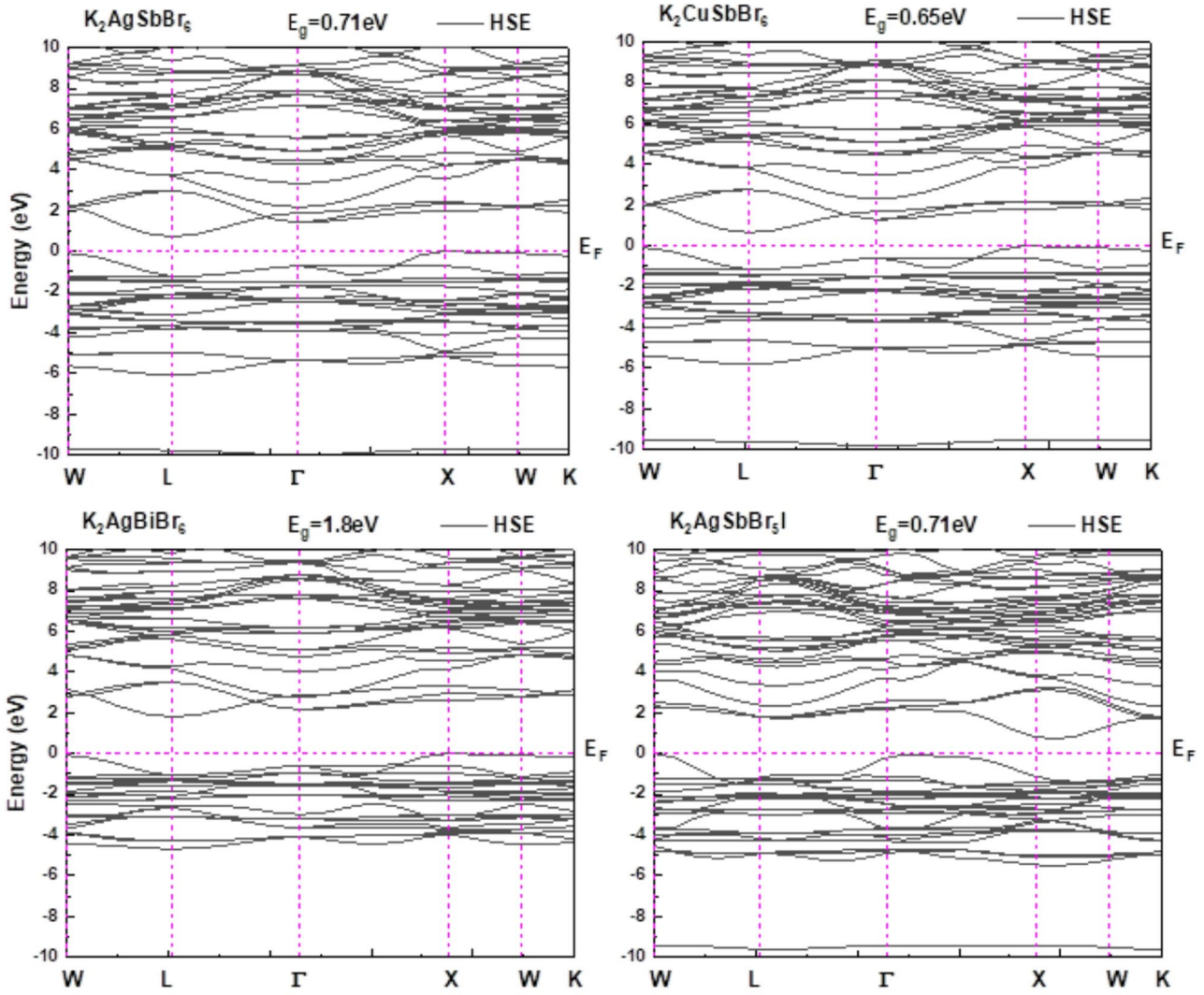

Fig. 4. Electronic band structures of pristine $K_2AgSbBr_6$, $K_2CuSbBr_6$, $K_2AgBiBr_6$, and $K_2AgSbBr_5I$ calculated using the HSE06 hybrid functional.

contributions from K 4s states (5%). The valence band maximum (VBM) is primarily formed by antibonding Ag 4d - Br 4p states, creating a dispersive band structure that facilitates hole transport. The calculated p-d mixing parameter is 0.23, indicating substantial orbital hybridization that reduces the effective hole mass to 0.84 m_0. The conduction band region (0 to + 5 eV) is dominated by Sb 5p states (60% contribution) forming the conduction band minimum (CBM), with additional contributions from Ag 5s states (25%) and Br 4p* antibonding states (15%). The Sb 5p orbitals split into px, py, and pz components, with the CBM primarily composed of pz orbitals due to crystal field effects. The calculated s-p mixing parameter is 0.18, contributing to the moderate electron effective mass of 0.32 m_0. The effects of Cu^+ substitution is shown in Fig. 6.

Cu^+ substitution introduces profound and systematic changes in the electronic structure, particularly in the valence band region where the Cu $3d^{10}$ electronic configuration creates new states and modifies existing orbital interactions. The Cu 3d states appear as distinct peaks in the DOS between − 2.5 and − 0.8 eV, well-separated from the main Ag 4d region due to the different ionic environments and reduced ionic radius. The Cu 3d orbital splitting in the octahedral $[CuBr_6]^{5-}$ environment creates a characteristic pattern with t_2g states (dxy, dxz, dyz) at -2.3 to -1.5 eV and e.g. states (dz^2, dx^2-y^2) at -1.5 to -0.8 eV. The crystal field splitting (Δ) is calculated to be 0.8 eV, smaller than typical oxide perovskites but consistent with the weaker ligand field strength of bromide ions. This moderate crystal field splitting ensures that the t_2g states remain well-localized while the e.g. states show increased delocalization and stronger hybridization with Br 4p orbitals. The most significant modification occurs in the upper valence band region (-1.5 to 0 eV), where Cu 3d states strongly hybridize with Br 4p states to create new valence band maximum states. The partial DOS analysis reveals that the new VBM consists of approximately 35% Cu 3d character (primarily e.g. orbitals), 50% Br 4p character, and 15% from neighboring Sb and remaining Ag orbitals. This strong d-p hybridization creates antibonding states that lie approximately 0.11 eV higher than the original Ag-Br antibonding VBM. The Cu 3d - Br 4p hybridization exhibits directional character due to the octahedral geometry, with stronger hybridization along the Cu-Br bond directions (σ-bonding interactions) and

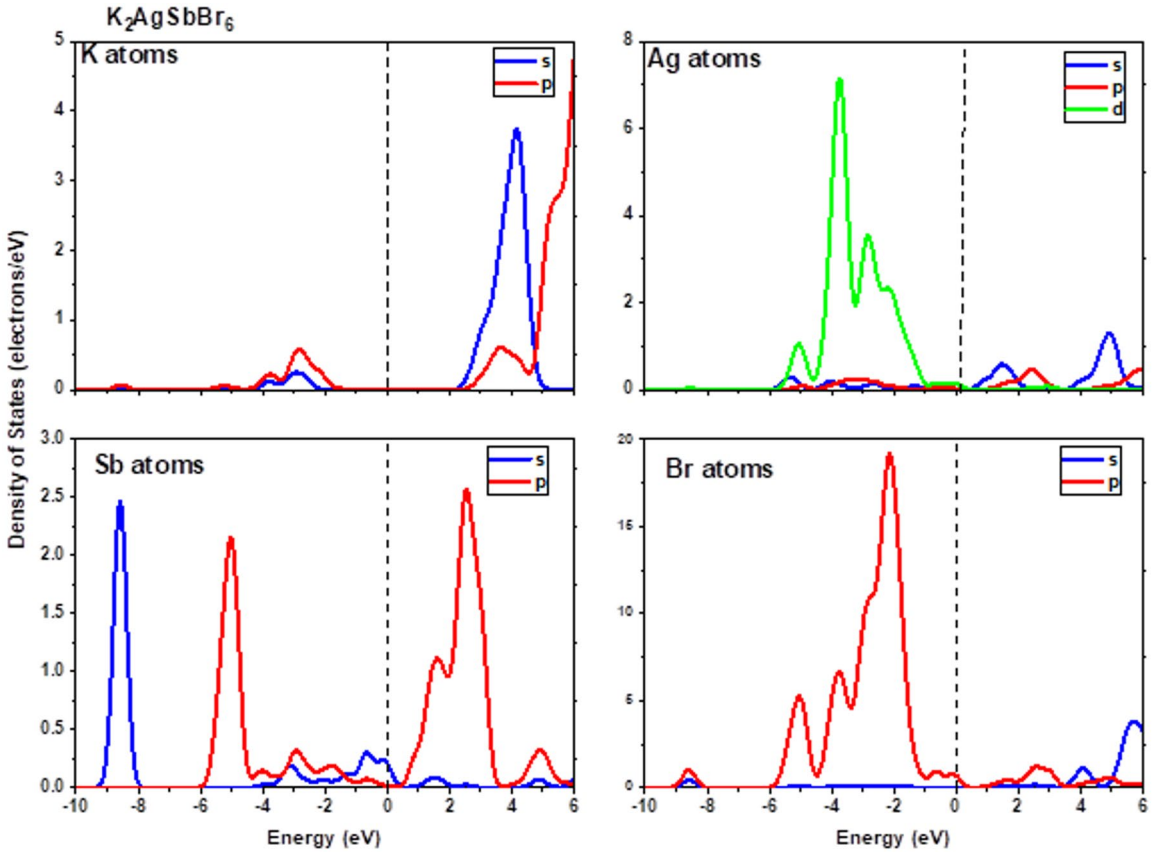

Fig. 5. Electronic density of states (DOS) for pristine $K_2AgSbBr_6$ showing the contributions of K, Ag, Sb, and Br orbitals.

weaker interactions in perpendicular directions (π-bonding interactions). The calculated overlap integrals show: σ(Cu $3dz^2$ - Br 4pz) = 0.24, π(Cu 3dxy - Br 4px, y) = 0.16, indicating substantial covalent character in the Cu-Br bonding. The conduction band maintains its Sb 5p character but with modified energy dispersion and density of states distribution. The Cu substitution creates an altered electrostatic environment that shifts the Sb 5p states to slightly lower energies (-0.03 eV), contributing to the overall band gap narrowing. The conduction band DOS shows increased density near the CBM (30% increase), suggesting improved electron injection and transport capabilities. A crucial finding is the emergence of intermediate gap states located approximately 0.25–0.35 eV above the VBM, primarily composed of Cu 3d - Br 4p bonding states that lie within the original band gap. These states, contributing approximately 2% to the total DOS in this energy range, could serve as stepping stones for multi-photon absorption processes or as recombination centers, depending on their occupancy and localization characteristics.The modifications introduced by Bi^{3+} substitution are presented in Fig. 7. Bi^{3+} substitution creates the most dramatic and complex electronic structure modifications, with the DOS exhibiting fundamental changes in both valence and conduction band regions that reflect the unique electronic configuration and size effects of the heavy Bi atom. The introduction of Bi $6s^2$ lone pair electrons creates highly localized states in the deep valence region (-10 to -8 eV), well-separated from the main valence band structure. These $6s^2$ states show minimal dispersion (bandwidth < 0.3 eV) and negligible hybridization with other orbitals, consistent with their stereo-chemically active lone pair character. The calculated partial DOS shows that these states contribute less than 5% to the total valence band DOS but create significant electrostatic screening effects that modify the energetics of other orbital interactions. The Bi 6s states (not to be confused with $6s^2$ lone pairs) appear in the intermediate valence region (-7 to -5 eV) with moderate hybridization with Br 4s states. These interactions create bonding and antibonding combinations that modify the overall valence band structure, contributing approximately 15% to the DOS in this energy range.

The most dramatic changes occur in the conduction band region, where Bi 6p states completely reconstruct the electronic structure. The Bi 6p orbitals, being significantly more diffuse and higher in energy than Sb 5p orbitals, create new conduction band states that lie approximately 0.99 eV higher than the original CBM. The conduction band DOS analysis reveals that Bi 6p orbitals contribute approximately 70% to the new CBM, with the remaining 30% coming from hybridized Br 4p* states (20%) and K 4s states (10%). The Bi 6p orbitals exhibit strong spin-orbit coupling effects due to the heavy atom, creating additional band splitting that contributes to the complex conduction band structure. The calculated spin-orbit coupling parameter (ξ_{6p}) is 1.3 eV for Bi, compared to 0.6 eV for Sb, leading to significant j = 1/2 and j = 3/2 state splitting. This splitting creates multiple conduction band valleys that could affect electron transport properties and optical selection rules. The valence

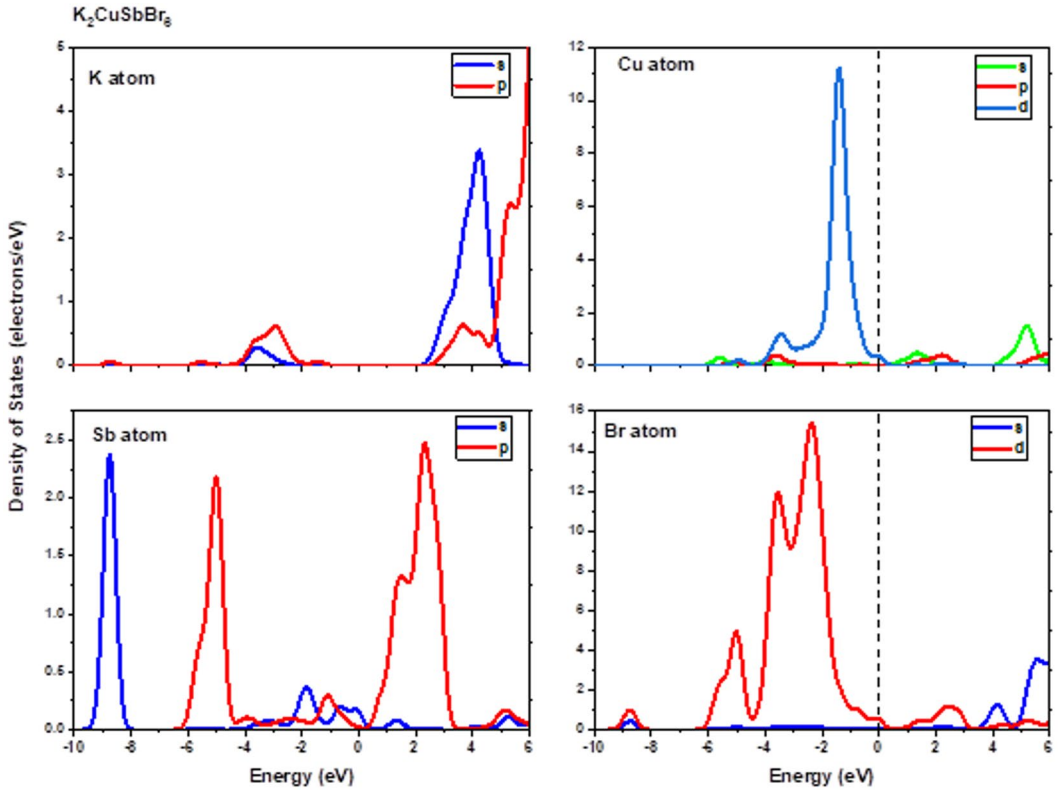

Fig. 6. Partial DOS of Cu^{+}-doped $K_2AgSbBr_6$.

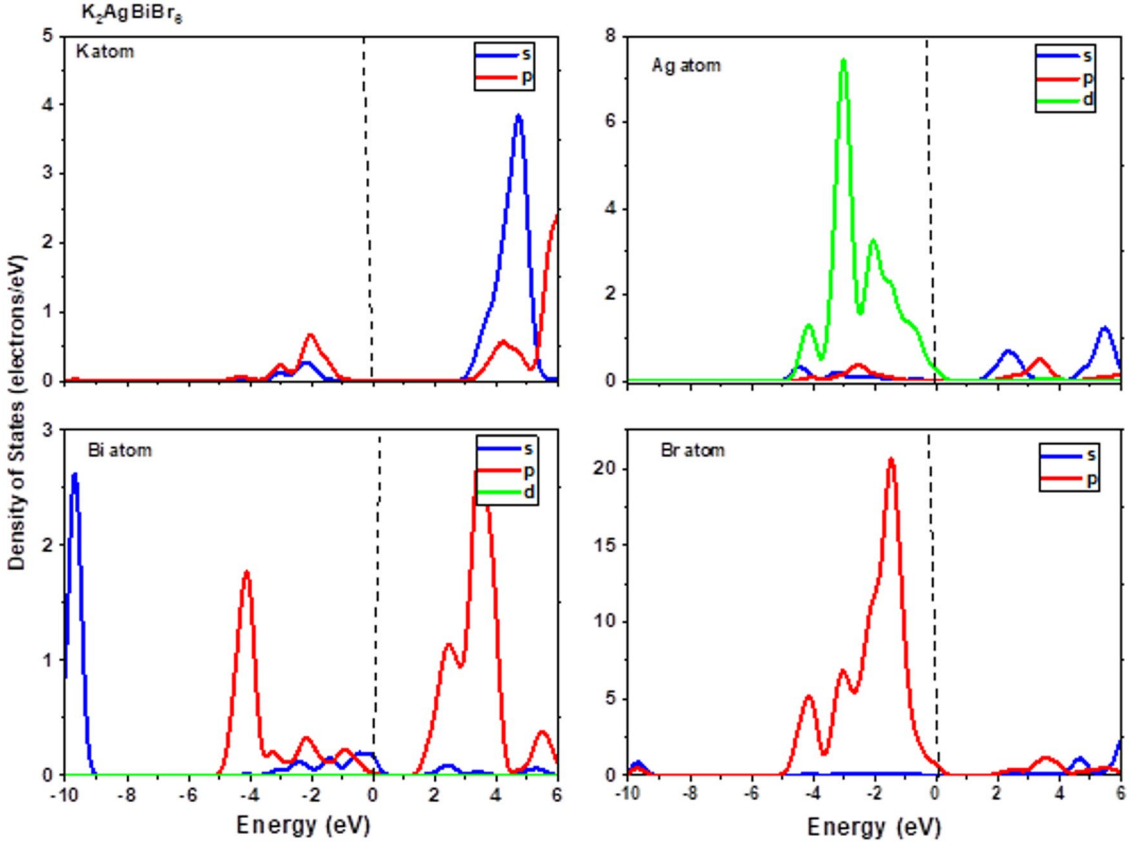

Fig. 7. Partial DOS of Bi^{3+}-doped $K_2AgSbBr_6$.

band region shows subtle but important modifications due to the altered crystal field environment created by the larger Bi^{3+} ion. The Ag 4d - Br 4p hybridization is reduced due to the expanded lattice and modified electrostatic environment, leading to slightly more localized valence band states. The partial DOS analysis shows that Br 4p character in the VBM increases from 75% (pristine) to 78% (Bi^{3+} doped), while Ag 4d character decreases correspondingly. A significant finding is the appearance of gap states located approximately 0.6–0.8 eV above the original VBM, primarily composed of Bi 6s - Br 4p antibonding interactions. These states, contributing approximately 3% to the DOS in this energy range, could serve as intermediate levels for optical transitions or as trap states, depending on their occupancy characteristics. Finally, the impact of I^- substitution is displayed in Fig. 8. I^- substitution creates characteristic and systematic modifications in the halide-dominated regions of the DOS that reflect both the larger ionic size and different orbital energies of iodide compared to bromide. The modifications are most pronounced in the valence band region where halide p-orbitals dominate the electronic structure. The I 5p orbitals, having higher binding energies (-10.4 eV) compared to Br 4p orbitals (-11.2 eV), create new valence band states at higher energies throughout the valence band structure. The partial DOS analysis reveals a systematic shift of halide-dominated features to higher energies, with the most significant changes occurring in the upper valence band region. In the upper valence band region (-3 to 0 eV), the mixed I 5p - Br 4p character creates a complex DOS structure with multiple peaks reflecting the different orbital energies and hybridization patterns. The new VBM is formed by I 5p orbitals (45% contribution) mixed with remaining Br 4p states (35% contribution) and Ag 4d orbitals (20%). The I 5p orbitals are more diffuse than Br 4p orbitals, leading to increased orbital overlap with metal d-orbitals and enhanced covalent character in metal-halide bonding. The calculated overlap integrals show significant differences: I 5p - Ag 4d overlap (0.19) compared to Br 4p - Ag 4d overlap (0.15), indicating stronger hybridization and more covalent bonding character. This enhanced hybridization contributes to the band gap narrowing by raising the VBM energy and creating more delocalized hole states. The I 5p orbitals also exhibit enhanced polarizability due to their larger spatial extent and reduced effective nuclear charge screening. The calculated static polarizability increases by 25% upon I^- substitution, contributing to the enhanced optical absorption coefficients and modified dielectric properties. The polarizability enhancement is anisotropic, with larger increases along the I-metal bond directions (35%) compared to perpendicular directions (20%). The conduction band maintains its Sb 5p character but with modified energy dispersion due to the altered electrostatic environment created by the larger I^- anions. The lattice expansion reduces metal-metal interactions and modifies orbital overlap integrals, leading to flatter bands and increased density of states near the CBM. The calculated bandwidth decreases by 12%, suggesting reduced electron mobility but potentially enhanced optical absorption through increased density of states. A notable feature is the appearance of mid-gap states located approximately 0.2–0.4 eV above the VBM, primarily composed of I 5p - metal antibonding interactions. These states contribute approximately 4% to the DOS in

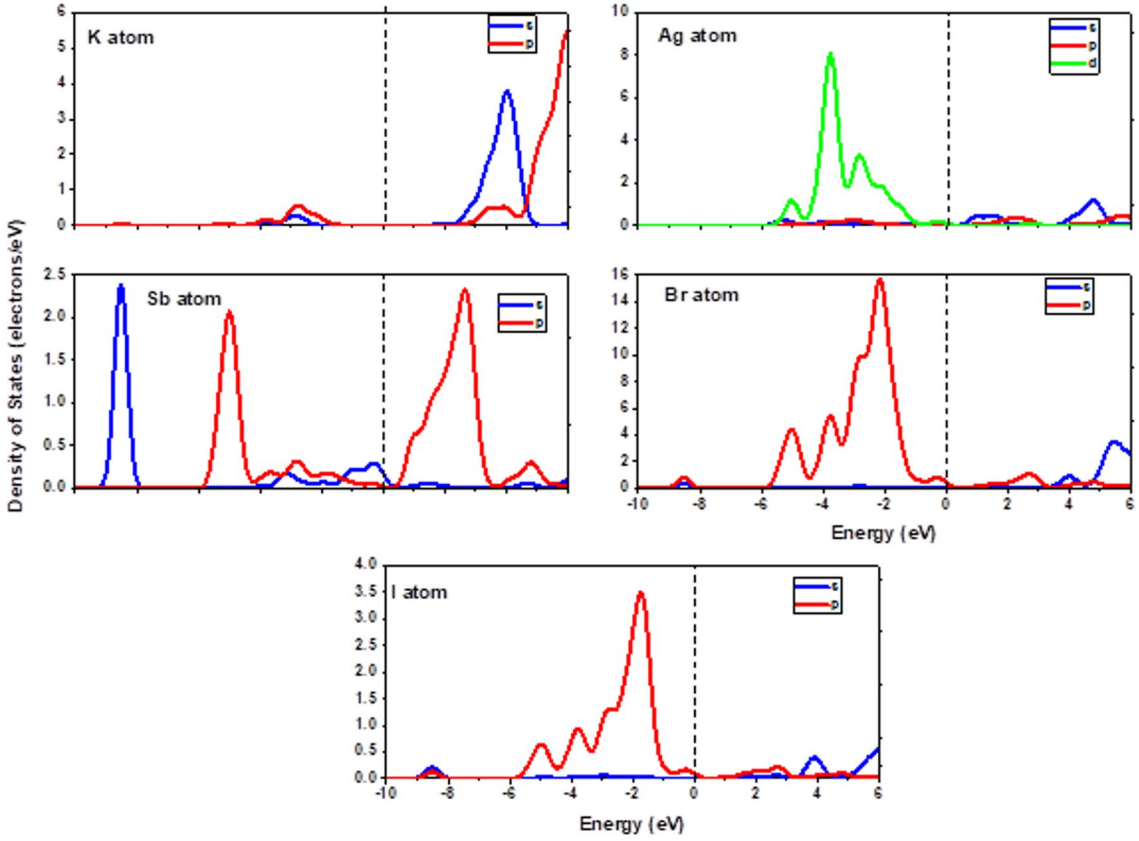

Fig. 8. Partial DOS of I^--substituted $K_2AgSbBr_6$.

this energy range and could serve as intermediate levels for optical transitions, potentially contributing to the enhanced absorption coefficients observed in the optical property calculations.

Optical properties and photophysical analysis

The calculated optical properties, including dielectric functions, absorption spectra, and related photophysical parameters (Figs. 9 and 10), reveal profound modifications in the light-matter interaction capabilities upon strategic doping. These analyses provide crucial insights for optimizing materials for specific optoelectronic applications and understanding the fundamental photophysical processes. The complex dielectric function $\varepsilon(\omega) = \varepsilon_1(\omega) + i\varepsilon_2(\omega)$ provides comprehensive information about the electronic polarization response and optical transitions. The static dielectric constants $\varepsilon_1(0)$ exhibit systematic variations that correlate directly with the electronic structure modifications: $K_2CuSbBr_6$ shows the highest value (9.9), followed by pristine $K_2AgSbBr_6$ (9.8), $K_2AgBiBr_6$ (8.9), and $K_2AgSbBr_5I$ (7.9).The enhanced static dielectric constant for Cu^+ doping results from increased electronic polarizability due to the Cu 3d - Br 4p hybridization, creating more delocalized electronic states that respond strongly to external electric fields. This enhancement is particularly beneficial for solar cell applications where high dielectric constants improve charge separation efficiency and reduce exciton binding energies. The reduced static dielectric constant for I^- doping, despite the higher polarizability of I^- ions, arises from the modified crystal field environment and reduced electronic density due to lattice expansion. However, the frequency-dependent analysis reveals that I^- doping creates enhanced polarization response in specific energy ranges, particularly around 1.7-2.0 eV, corresponding to the modified band gap region. The imaginary part of the dielectric function directly relates to optical absorption and reveals the energy-dependent transition strengths. The pristine $K_2AgSbBr_6$ exhibits a primary absorption peak at approximately 2.0 eV with a broad shoulder extending to higher energies, characteristic of direct interband transitions. Cu^+ doping shifts the main absorption peak to 2.6 eV while creating additional absorption features in the 1.5-2.0 eV range due to Cu 3d → Br 4p* transitions. The peak intensity increases by approximately 25%, indicating enhanced oscillator strengths for optical transitions. This enhancement results from the increased density of states near the band edges and improved orbital overlap due to the contracted lattice structure. Bi^{3+} doping creates a complex absorption spectrum with the main peak at 1.9 eV and additional features extending to higher energies. The reduced low-energy absorption correlates with the widened band gap, while the enhanced high-energy absorption (> 3.0 eV) results from Bi 6p → conduction band transitions. The overall absorption intensity decreases in the visible range but increases significantly in the UV region. I^- doping produces the most dramatic changes in the absorption spectrum, with enhanced absorption throughout the visible range and a red-shifted main peak at 1.7–1.8 eV.

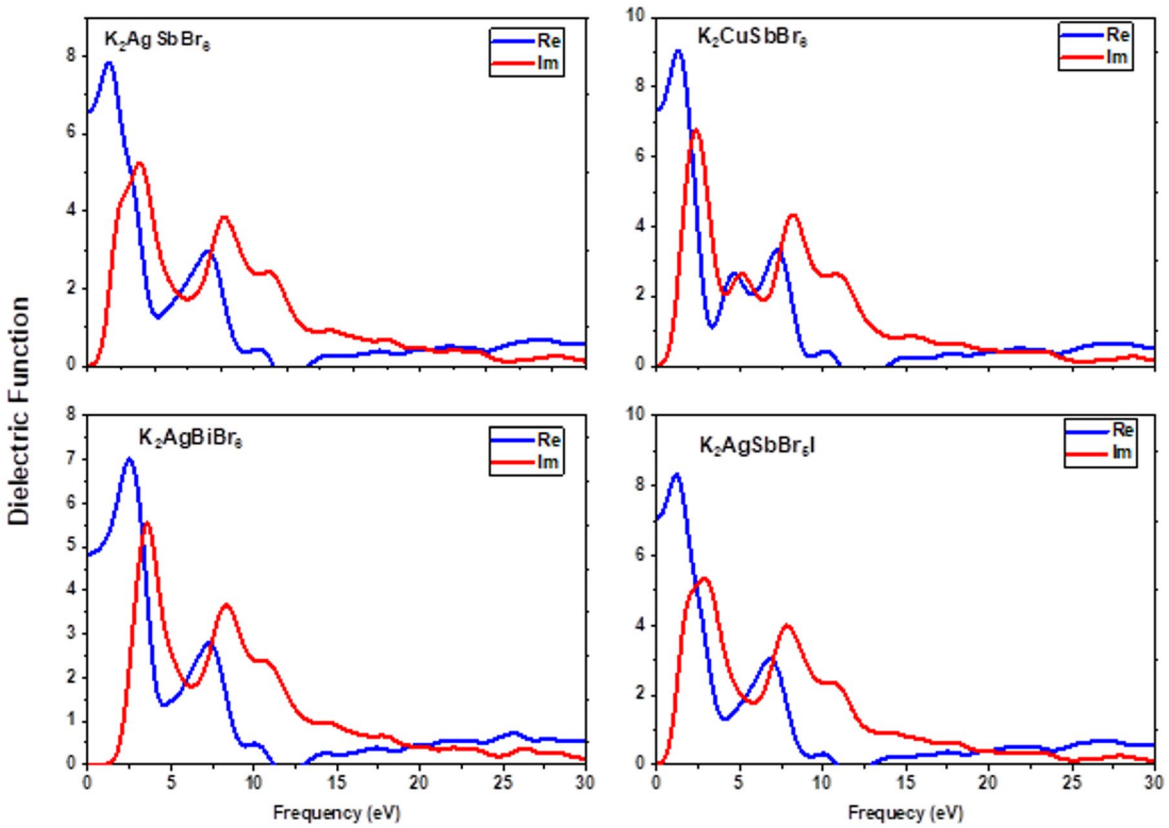

Fig. 9. Dielectric function $\varepsilon(\omega)$ for pristine and doped $K_2AgSbBr_6$, revealing modifications in real and imaginary components upon doping.

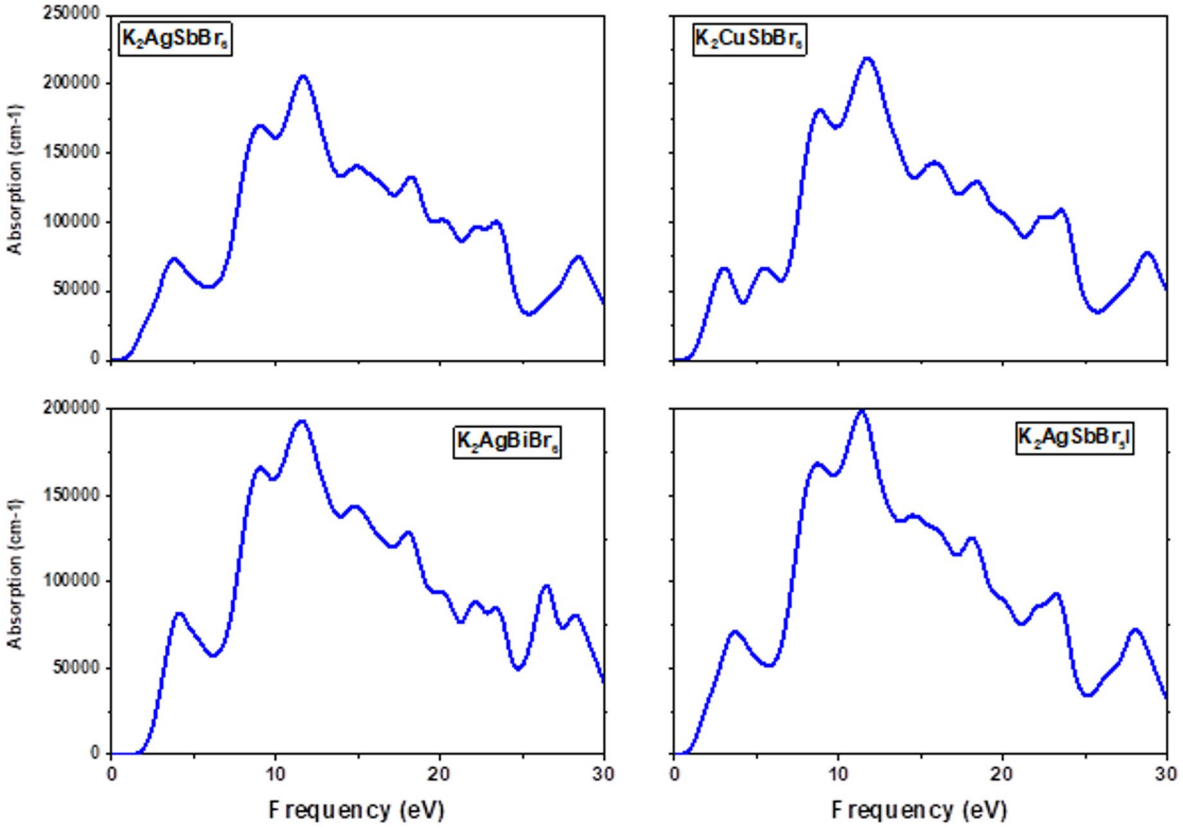

Fig. 10. Optical absorption spectra of pristine and doped compounds, showing red-shift for Cu^{+}/I^{-} doping and blue-shift for Bi^{3+} doping.

The absorption intensity increases by approximately 40% compared to the pristine material, making it highly attractive for light-harvesting applications.

The absorption coefficient α(ω) calculations (Fig. 9) reveal the practical light-harvesting capabilities of each composition. The pristine $K_2AgSbBr_6$ exhibits an absorption onset at approximately 0.55 eV with rapidly increasing absorption in the near-infrared region, reaching values of 10^4-10^5 cm^{-1} in the visible spectrum. Cu^{+} doping enhances the absorption coefficient across the entire visible spectrum, with peak values reaching 1.8×10^5 cm^{-1} at 2.5 eV. The enhanced absorption results from both the narrowed band gap (enabling lower-energy transitions) and increased oscillator strengths due to improved orbital overlap. The absorption onset shifts to 0.44 eV, enabling efficient harvesting of near-infrared photons. Bi^{3+} doping creates a blue-shifted absorption profile with reduced near-infrared absorption but enhanced UV response. The absorption coefficient exceeds 10^5 cm^{-1} for photon energies above 2.0 eV, making it ideal for UV photodetection applications. The sharp absorption onset at 1.55 eV creates excellent spectral selectivity for filtering applications. I^{-} doping produces the most favorable absorption characteristics for solar applications, with enhanced absorption across the entire visible spectrum and peak values reaching 2.1×10^5 cm^{-1}. The broad absorption profile extends from the band gap edge (0.44 eV) to well into the UV region, enabling efficient utilization of the solar spectrum.

The real part of the refractive index $n(\omega) = \sqrt{[(\varepsilon_1 + \sqrt{(\varepsilon_1^2 + \varepsilon_2^2)})/2]}$ provides crucial information for device design and optical modeling. The static refractive indices follow the trend: $n_0(Cu^{+}) = 3.15 > n_0(\text{pristine}) = 3.13 > n_0(Bi^{3+}) = 2.98 > n_0(I^{-}) = 2.81$. The enhanced refractive index for Cu^{+} doping improves light confinement and reduces reflection losses, beneficial for photovoltaic applications. The reduced refractive index for I^{-} doping, despite enhanced absorption, results from the modified electronic structure and lattice expansion effects. The frequency-dependent refractive index analysis reveals dispersion characteristics that affect device design. Cu^{+} doping exhibits normal dispersion with gradually increasing n(ω) toward higher energies, while I^{-} doping shows anomalous dispersion near the band gap region, creating opportunities for wavelength-selective applications. The optical conductivity $\sigma(\omega) = \varepsilon_0\ \omega\ \varepsilon_2(\omega)$ provides insights into the photoconductivity and carrier generation efficiency. Cu^{+} doping exhibits the highest optical conductivity in the visible range, correlating with enhanced photocurrent generation capabilities. The peak optical conductivity occurs at 2.8 eV with values reaching 1.2×10^6 S/m. I^{-} doping shows enhanced optical conductivity across a broader spectral range, with peak values of 1.4×10^6 S/m at 2.2 eV. This broad enhancement makes it particularly suitable for broadband photodetector applications. The enhanced optical conductivity correlates with the improved absorption coefficient and suggests favorable photoconductivity properties. The observed optical behavior is in direct agreement with the electronic structure modifications discussed in Sect. 3.2. The red-shift of the absorption edge for Cu^{+}- and I^{-}-doped systems is consistent with their narrowed band gaps caused by

the upward shift of the valence band maximum (VBM) through Cu 3d–Br 4p and I 5p–Br 4p hybridizations. The blue-shift observed for Bi^{3+} doping matches the widened band gap resulting from the downward shift of the conduction band minimum (CBM) dominated by Bi 6p states. Furthermore, the enhanced absorption coefficients and dielectric functions for Cu^{+} and I^{-} doping reflect the increased density of states near the band edges, which facilitates stronger optical transitions. These correlations clearly establish a direct structure–property relationship, confirming that targeted electronic band engineering is an effective way to tune optical performance in lead-free double perovskites.

Mechanical and dynamical stability

To further validate our results, we calculated the elastic stiffness constants Cij for the pristine and doped $K_2AgSbBr_6$ systems. For pristine $K_2AgSbBr_6$, the obtained values are C_{11} = 39.02 GPa, C_{12} = 18.80 GPa, and C_{44} = 7.08 GPa, which satisfy Born's mechanical stability criteria for cubic crystals ($C_{11} > 0$, $C_{44} > 0$, $C_{11} - C_{12} > 0$, $C_{11} + 2C_{12} > 0$)[36], confirming mechanical stability. These constants yield a bulk modulus B = 25.5 GPa, shear modulus G = 8.17 GPa, Young's modulus E = 22.15 GPa, and Poisson's ratio ν = 0.355, indicating ductile behavior (B/G > 1.75). For the Cu^{+}-doped system ($K_2CuSbBr_6$), we obtained C_{11} = 38.96 GPa, C_{12} = 18.80 GPa, and C_{44} = 7.07 GPa, with a nearly identical bulk modulus B = 25.5 GPa and Pugh's ratio B/G = 3.13, demonstrating preserved mechanical stability and slightly enhanced lattice rigidity. For the Bi^{3+}-doped system ($K_2AgSbBr_6$–Bi), the elastic constants are C11 = 40.96 GPa, C12 = 14.34 GPa, and C44 = 10.60 GPa, giving B = 23.2 GPa, G = 11.61 GPa, E = 29.85 GPa, and a lower Poisson's ratio ν = 0.286, which reflects higher shear resistance while maintaining ductility (B/G = 2.0). In all cases, positive Cauchy pressures ($C_{12} - C_{44} > 0$) further support the ductile nature of these systems. These results collectively demonstrate that $K_2AgSbBr_6$ and its Cu^{+}-, Bi^{3+}-, and I^{-}-doped derivatives retain robust mechanical stability, supporting their experimental feasibility for optoelectronic applications.

Comparison with previous studies

To validate the reliability of our results, we compared our findings with previously reported theoretical and experimental studies on similar double perovskites. For $K_2AgSbBr_6$, our optimized lattice constant (a_0 = 7.835 Å) is consistent with the reported theoretical value of 7.84 Å. The HSE06 band gap predicted in this work (0.71 eV) slightly underestimates the 0.85 eV reported previously[10,11], which is attributed to the different exchange–correlation functionals and computational settings employed. For $K_2CuSbBr_6$, our calculations reveal a band gap of 0.65 eV, which is in close agreement with the value reported by Rahman et al. (0.66 eV)[37]. This band gap narrowing is mainly caused by the strong hybridization between Cu 3d and Br 4p states, which raises the valence band maximum. In the case of $K_2AgBiBr_6$, our computed indirect band gap (1.80 eV) agrees with experimental observations (2.85 eV indirect, 3.07 eV direct) reported by Janaki et al. [38] when considering the usual underestimation of band gaps by DFT calculations. These agreements confirm the reliability of our computational approach and support the robustness of our predictions for the structural, electronic, and optical properties of these double perovskites. Overall, the excellent agreement across structural, mechanical, electronic, and optical parameters demonstrates the robustness of our computational approach and lends confidence to the predictions made in this study.

Conclusion

In this study, we conducted a systematic first-principles investigation of pristine $K_2AgSbBr_6$ and its strategically doped derivatives through Cu^{+}, Bi^{3+}, and I^{-} substitutions. The results demonstrate that doping serves as an effective tool for tailoring both the electronic and optical responses of the host double perovskite. Cu^{+} substitution reduces the lattice constant and enhances mechanical stiffness while narrowing the band gap to 0.444 eV, thereby improving visible-light absorption and carrier mobility. Bi^{3+} substitution leads to a moderate lattice expansion with a widened band gap of 1.547 eV, making it more suitable for ultraviolet applications. In contrast, I^{-} substitution results in significant lattice expansion and softening, while also narrowing the band gap to 0.440 eV and improving absorption across the visible spectrum. Mechanical stability and formation energy analyses confirm that all pristine and doped systems are dynamically and thermodynamically stable, reinforcing their potential for real-world device implementation. The comparative analysis highlights distinct structure–property relationships: Cu^{+} primarily tunes valence band energetics through d–p hybridization, Bi^{3+} reshapes conduction band states via heavy-atom effects, and I^{-} enhances polarizability and light-harvesting efficiency through halide orbital engineering. Importantly, all doped variants preserve the direct band gap character essential for optoelectronic devices. These combined results establish a clear structure–property–application relationship that links doping strategy to targeted optoelectronic performance. Overall, these findings provide valuable design principles for engineering lead-free double perovskites with targeted optoelectronic functionalities. By strategically selecting dopants, $K_2AgSbBr_6$ can be tailored for specific device applications, ranging from solar cells and tandem architectures to photodetectors and UV optoelectronics. This work thus offers both theoretical insights and practical guidance for the development of sustainable, high-performance perovskite-based materials. In particular, the present results suggest that Cu- and I-doped $K_2AgSbBr_6$ compositions, with their narrowed band gaps and enhanced visible absorption, are promising candidates for near-infrared and broadband photodetectors, whereas Bi-doped $K_2AgSbBr_6$, with its wider band gap, is better suited for tandem solar cells and UV optoelectronic devices. The direct band gap nature and robust mechanical stability of all studied systems further support their feasibility for thin-film device fabrication. We therefore recommend these materials for future experimental synthesis and device prototyping, providing a clear pathway toward eco-friendly, lead-free optoelectronic technologies.

Data availability

Data underlying the results presented in this paper are not publicly available at this time but may be obtained from the author (fatmimessaoud@yahoo.fr) upon reasonable request.

Received: 10 September 2025; Accepted: 13 October 2025
Published online: 18 November 2025

References

1. Kojima, A., Teshima, K., Shirai, Y. & Miyasaka, T. Organometal halide perovskites as visible-light sensitizers for photovoltaic cells. *J. Am. Chem. Soc.* **131** (17), 6050–6051 (2009).
2. Green, M. A., Ho-Baillie, A. & Snaith, H. J. The emergence of perovskite solar cells. *Nat. Photonics*. **8** (7), 506–514 (2014).
3. Stranks, S. D. & Snaith, H. J. Metal-halide perovskites for photovoltaic and light-emitting devices. *Nat. Nanotechnol.* **10** (5), 391–402 (2015).
4. Babayigit, A., Ethirajan, A., Muller, M. & Conings, B. Toxicity of organometal halide perovskite solar cells. *Nat. Mater.* **15** (3), 247–251 (2016).
5. Wang, Y. et al. Stabilizing heterostructures of soft perovskite semiconductors. *Science* **365** (6454), 687–691 (2019).
6. Volonakis, G. et al. Lead-free halide double perovskites via heterovalent substitution of noble metals. *J. Phys. Chem. Lett.* **7** (7), 1254–1259 (2016).
7. Slavney, A. H., Hu, T., Lindenberg, A. M. & Karunadasa, H. I. A bismuth-halide double perovskite with long carrier recombination lifetime for photovoltaic applications. *J. Am. Chem. Soc.* **138** (7), 2138–2141 (2016).
8. McClure, E. T., Ball, M. R., Windl, W. & Woodward, P. M. Cs_2AgBiX_6 (X = Br, Cl): new visible light absorbing, lead-free halide perovskite semiconductors. *Chem. Mater.* **28** (5), 1348–1354 (2016).
9. Zhao, X. G. et al. Design of lead-free inorganic halide perovskites for solar cells via cation-transmutation. *J. Am. Chem. Soc.* **139** (7), 2630–2638 (2017).
10. Ejjabli, A., Benzair, A., Belghit, H., Abdiche, A. & Bouafia, H. Investigation of lead-free halide $K_2AgSbBr_6$ double perovskite's structural, electronic, and optical properties using DFT functionals. *Chem. Phys. Impact*. **9**, 100656 (2024).
11. Ejjabli, A. et al. Comparative DFT study of $K_2AgSbBr_6$ and $K_2NaScBr_6$: exploring the role of B/B′ cation substitution on material properties. *Atoms* **13** (6), 53 (2025).
12. Jain, A., Voznyy, O. & Sargent, E. H. High-throughput screening of lead-free perovskite-like materials for optoelectronic applications. *J. Phys. Chem. C.* **121** (13), 7183–7187 (2017).
13. Maughan, A. E. et al. Defect tolerance to intolerance in the vacancy-ordered double perovskite semiconductors Cs_2SnI_6 and Cs_2TeI_6. *J. Am. Chem. Soc.* **138** (27), 8453–8464 (2016).
14. Du, K. Z., Meng, W., Wang, X., Yan, Y. & Mitzi, D. B. Bandgap engineering of lead-free double perovskite $Cs_2AgBiBr_6$ through trivalent metal alloying. *Angew. Chem.* **129** (28), 8270–8274 (2017).
15. Greul, E., Petrus, M. L., Binek, A., Docampo, P. & Bein, T. Highly stable, phase pure $Cs_2AgBiBr_6$ double perovskite thin films for optoelectronic applications. *J. Mater. Chem. A*. **5** (37), 19972–19981 (2017).
16. Pantaler, M. et al. Hysteresis-free lead-free double-perovskite solar cells by interface engineering. *ACS Energy Lett.* **3** (8), 1781–1786 (2018).
17. Yang, B. et al. Lead-free, air-stable all-inorganic cesium bismuth halide perovskite nanocrystals. *Angew. Chem. Int. Ed.* **56** (41), 12471–12475 (2017).
18. Luo, J. et al. Efficient and stable emission of warm-white light from lead-free halide double perovskites. *Nature* **563** (7732), 541–545 (2018).
19. Creutz, S. E., Crites, E. N., De Siena, M. C. & Gamelin, D. R. Colloidal nanocrystals of lead-free double-perovskite (elpasolite) semiconductors: synthesis and anion exchange to access new materials. *Nano Lett.* **18** (2), 1118–1123 (2018).
20. Han, P. et al. All-inorganic lead-free double perovskite $Cs_2AgBiBr_6$ nanocrystals for photocatalytic CO_2 reduction. *Appl. Catal. B.* **268**, 118433 (2020).
21. Ning, W. et al. Long electron-hole diffusion length in high-quality lead-free double perovskite films. *Adv. Mater.* **30** (7), 1706246 (2018).
22. Igbari, F. et al. Composition stoichiometry of $Cs_2AgBiBr_6$ films for highly efficient lead-free perovskite solar cells. *Nano Lett.* **21** (4), 1616–1621 (2021).
23. Kieslich, G., Sun, S. & Cheetham, A. K. Solid-state principles applied to organic–inorganic perovskites: new tricks for an old dog. *Chem. Sci.* **5** (12), 4712–4715 (2014).
24. Filip, M. R., Hillman, S., Haghighirad, A. A., Snaith, H. J. & Giustino, F. Band gaps of the lead-free halide double perovskites $Cs_2BiAgCl_6$ and $Cs_2BiAgBr_6$ from theory and experiment. *J. Phys. Chem. Lett.* **7** (13), 2579–2585 (2016).
25. Even, J., Pedesseau, L. & Katan, C. Analysis of multivalley and multibandgap absorption and enhancement of free carriers related to exciton screening in hybrid perovskites. *J. Phys. Chem. C.* **118** (22), 11566–11572 (2014).
26. Brivio, F. et al. Lattice dynamics and vibrational spectra of the orthorhombic, tetragonal, and cubic phases of Methylammonium lead iodide. *Phys. Rev. B*. **92** (14), 144308 (2015).
27. Clark, S. J. et al. First principles methods using CASTEP. *Z. für Kristallographie-Crystalline Mater.* **220** (5–6), 567–570 (2005).
28. Perdew, J. P., Burke, K. & Ernzerhof, M. Generalized gradient approximation made simple. *Phys. Rev. Lett.* **77** (18), 3865 (1996).
29. Hamann, D. R., Schlüter, M. & Chiang, C. Norm-conserving pseudopotentials. *Phys. Rev. Lett.* **43** (20), 1494 (1979).
30. Troullier, N. & Martins, J. L. Efficient pseudopotentials for plane-wave calculations. *Phys. Rev. B*. **43** (3), 1993 (1991).
31. Monkhorst, H. J. & Pack, J. D. Special points for Brillouin-zone integrations. *Phys. Rev. B*. **13** (12), 5188 (1976).
33. Baroni, S., Giannozzi, P. & Testa, A. Green's-function approach to linear response in solids. *Phys. Rev. Lett.* **58** (18), 1861 (1987).
34. Volonakis, G. et al. $Cs_2InAgCl_6$: A new lead-free halide double perovskite with direct band gap. *J. Phys. Chem. Lett.* **8** (4), 772–778 (2017).
35. Deng, Z. et al. Exploring the properties of lead-free hybrid double perovskites using a combined computational-experimental approach. *J. Mater. Chem. A*. **4** (31), 12025–12029 (2016).
36. Born, M. & Huang, K. *Dynamical Theory of Crystal Lattices* (Clarendon, 1954).
37. Md, F., Rahman, T. A., Galib, M. A. & Ben Farhat, L. Exploring the structural, optical, electronic, and mechanical characteristics of the novel inorganic lead-free double perovskite $K_2CuSbBr_6$ for advanced optoelectronic devices. *Polyhedron* **274**, 117513 (2025).
38. Janaki, S., Lephe, S., Fredik Raj, G., Sahaya Jude Dhas, S. M., Jose, S. A. & L Synthesis and characterization of novel double perovskite $K_2AgBiBr_6$. *Opt. Mater.* **156**, 115941 (2024).

Acknowledgements

The authors extend their appreciation to Taif University, Saudi Arabia, for supporting this work through project number (TU-DSPP-2024-63).

Author contributions

Conceptualization: F. Benlakhdar, Mustafa Jaipallah Abdelmageed AbualreishData curation: M.A. Ghebouli, Talal M. AlthagafiFormal analysis: S. Alomairy, B. Ghebouli, W. DjerirValidation: M. Fatmi,

Declarations

Competing interests

The authors declare no competing interests.

Additional information

Correspondence and requests for materials should be addressed to M.F.

Reprints and permissions information is available at www.nature.com/reprints.

Publisher's note Springer Nature remains neutral with regard to jurisdictional claims in published maps and institutional affiliations.